2020 IEEE/RSJ International Conference on Intelligent Robots and Systems (IROS)
October 25-29, 2020, Las Vegas, NV, USA (Virtual)

Payload optimization of surgical instruments with rolling joint mechanisms

Dong-Ho Lee, Minho Hwang, Joonhwan Kim, and Dong-Soo Kwon

Abstract— **Many surgical robots with steerable surgical instruments have been proposed for endoscopic surgery. Surgical instruments should be small in size for insertion into the body and be able to handle large payloads such as tissue. Because the overall diameter and payload parameters are a trade-off, it is difficult to design an instrument with a large payload while reducing its diameter. In this paper, we optimize the payload of a rolling joint mechanism by deriving the moment equilibrium equation and constraints for endoscopic surgery. A scaled-up prototype was fabricated with the design variables obtained from the optimization, and the validity of the method for calculating the payload was confirmed by the experimentally measured payload. By plotting the distribution of payloads obtained from the moment equilibrium equation, we also confirmed that the payload obtained from the optimization is the maximum. In addition, optimizations with different numbers of joints confirm that the payload tends to decrease as the number of joints increases. This payload optimization method could also be extended to minimizing the deflection of the bending section against external forces and minimizing the diameter of the surgical instrument given the minimum required payload.**

I. Introduction

Endoluminal and transluminal endoscopic surgeries are surgeries in which an endoscope is inserted through natural openings such as the mouth, anus, or vagina instead of external incisions [1]. Because no external incisions are required, these types of surgery preserve aesthetics, decrease postoperative pain, and provide both rapid recovery and shorter hospitalization periods [2], [3].

Conventional endoscopes have a limited ability to perform surgery due to the lack DOFs (degrees of freedom) on their surgical tools. Advanced robotic platforms have been developed to achieve dexterous tissue manipulation capability, such as MASTER [4], ViaCath [5], i2Snake [6], and ease [7]. We previously proposed K-FLEX [8] and a robotic surgical instrument that can be attached onto a conventional endoscope [9]. These systems have additional steerable robotic surgical instruments to enable complex procedures and master devices to control the instruments. Most flexible instruments are driven by Bowden cables or other elastic materials to guarantee flexibility.

The instruments should be small in size to be inserted into natural openings, and strong sufficient to manipulate high payloads of organs at the same time. However, the diameter and pay- load parameters have a trade-off relationship. This is because the payload is generally proportional to the moment arm between the joint and the actuated wire, and the moment arm is proportional to the diameter of the joint. Most previous studies have not addressed the payload clearly. The systems were developed first, and the payload of the instrument was measured through experiments.

Many efforts have addressed to overcome the trade-off in continuum joints. Berthet-Rayne et al. [10] proposed the design optimization to prevent the tendons and joints from colliding during bending. However, the payload was not considered in their optimization. Butler et al. [11] have focused on deflection and proposed a method to reduce the amount of deflection of continuum against environmental loads. Some studies proposed methods to prevent shape distortion in flexible instruments. Tapered wire paths between each joint have been used to ensure that each joint has the same angle given an external force [12], [13]. Another study proposed an idea that, consecutive joints are mechanically constrained by auxiliary rolling links to prevent shape distortion and maximized the moment arm by routing the wire path outside the joints [14]. In spite of these efforts in continuum joints for surgical applications, neither of these studies have addressed optimizing design variables of the joint in perspective of payload capability.

In this paper, the payload of surgical instruments consisting of a rolling contact joint mechanism was analyzed and maximized by optimization of joint design variables. To confirm the validity of the optimization, we compare the calculated maximum payload and joint angles with respect to an input wire tension and the experimentally measured values in the scaled-up prototype. We also analyzed how frictional forces affect payloads and looked at changes in the payload optimization based on the number of joints.

II. Method

A. Flexible Surgical Instrument with Rolling Contact Joints

Most joints for a flexible surgical instrument can be categorized as continuum joints or hyper-redundant joints. Continuum joints use elastic structures such as elastic back-bones and slit tubes [15]-[19]. They can be bent continuously,

* This work was supported by the National Research Foundation (NRF) of Korea (Grant No. 2017H1A2A1043 159) and a grant from the International Joint Technology Development Project funded by the Korean Ministry of Trade, Industry and Energy (Grant No. P0006718)

Dong-Ho Lee is with the Robotics Program, Korea Advanced Institute of Science and Technology, Daejeon, 34141, South Korea vanquisher90@gmail.com

Minho Hwang is with the Department of Electrical Engineering and Computer Science, University of California Berkeley, California, 94720, USA gkgk1215@gmail.com

Joonhwan Kim is with the Department of Mechanical Engineering, Korea Advanced Institute of Science and Technology, Daejeon, 34141, South Korea joonhwan@kaist.ac.kr

Dong-Soo Kwon is with the Department of Mechanical Engineering, Korea Advanced Institute of Science and Technology, Daejeon, 34141, South Korea, He is also the CEO of EasyEndo Surgical Inc.

and thus they have an infinite number of DOFs. These joints can be miniaturized because they are actuated only by the structural inherent elasticity and wires. However, to resist the inherent elasticity, a large tension is required to bend the joints, which sometimes causes axial compression [20]. For this reason, these joints are not suitable for surgical instruments that must handle a large payload.

Hyper-redundant joints consist of a series of short and rigid parts, which can be further divided into ball joints [21]-[23] and rolling contact joints including pin joints [12]-[14], [24], [25]. The ball joints, which can be treated as short 2-DOF joints, can be miniaturized, but have low resistance against torsion and low utility because the ball takes up space in the middle of the joint. In contrast, a rolling contact joint rolls on the circular surface between two joints and can be actuated with wires without additional parts, so the rolling joints can be miniaturized and tooltips such as forceps and cautery can be inserted into the middle of the joint. For this reason, we focus on rolling contact joint mechanisms.

A bending section of a surgical instrument can be composed of single or a series of n rolling contact joints. In Figs. 1 and 2, the bending sections have one DOF. If the bending section has two DOFs, the joint is divided into two halves, and the split parts are replaced by a rolling contact joint for another DOF. The characteristics of the joint are determined by its shape, which depends on the following design variables: R is the radius of the rolling surface, B is the step depth of the wire hole from the top of the rolling surface, d is the distance from the center of the joint to the wire, θ_n is the rotation angle at the n^{th} joint, and H_n is the length of the n^{th} joint. For the convenience and visualization of calculation and manufacturing, all joints are constrained to be the same length except for the distal joint with the tooltip at the end. These variables determine the distance between the rolling contact point and the wire (D) as well as the exposed wire length between two adjacent joints (L), which are respectively expressed as

$$\mathrm{D_a}(\theta) = \mathrm{D_b}(-\theta) = d\cos\left(\frac{\theta}{2}\right) - (\mathrm{R}-\mathrm{B})\sin\left(\frac{\theta}{2}\right) \quad (1)$$

$$\mathrm{L_a}(\theta) = \mathrm{L_b}(-\theta) = 2R - 2d\sin\left(\frac{\theta}{2}\right) - 2(\mathrm{R}-\mathrm{B})\cos\left(\frac{\theta}{2}\right) \quad (2)$$

The subscript a indicates the bending direction, and the subscript b indicates the stretching direction. When the rolling joint moves from neutral to an angle θ, the total amount the wires shrink and stretch is expressed as (3). If R and B are the same, the total wire variation is zero, so the total length of the wire is always kept constant.

$$\begin{aligned}\Delta L &= [\mathrm{L_a}(\theta) - \mathrm{L_a}(0)] + [\mathrm{L_b}(\theta) - \mathrm{L_b}(0)] \\ &= 4(R-B)\left[1 - cos\left(\frac{\theta}{2}\right)\right]\end{aligned} \quad (3)$$

Force F is the horizontal force at the tip of the instrument and we define this as the payload. Further, tensions are applied on both wires. These payload and wire tensions have a functional relationship with joint angles. That is, when the input tensions are determined, the joint angles are determined by the payload. This relationship can be found by obtaining the moment equilibrium on the rolling contact points. The moment equilibrium is expressed as equation (4). It is assumed that there is no axial force at the tip in the equation

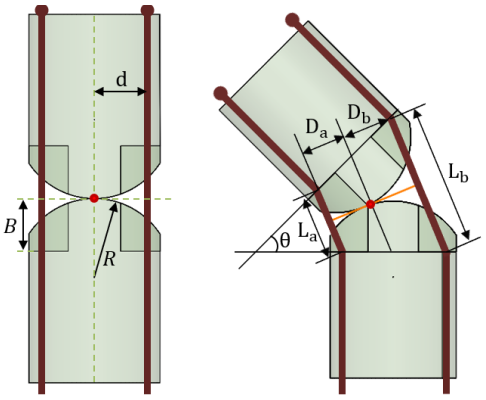

Fig. 1. Diagram of a single rolling contact joint

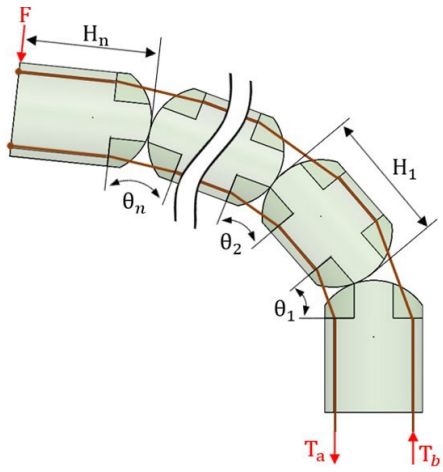

Fig. 2. Diagram of a bending section consisting of a series of n rolling contact joint

(4). In addition, it was assumed that there was no effect on the stiffness of the bending section, except for that on the wire.

$$\mathrm{F}\mathbf{U}\mathbf{h} + \mathbf{M} = 0 \quad (4)$$

In equation (4), $\mathbf{U}$ is a $(\mathrm{n}\times\mathrm{n})$ upper triangular matrix where all entries are 1, $\mathbf{h}$ is a $(\mathrm{n}\times 1)$ column vector where each row is h_i, which is the vertical distance to the payload direction between the rolling contact joints of the i^{th} and $(i+1)^{th}$ joints and the last h_n is the vertical distance in payload direction between the rolling contact point of the last joint and the tip. In addition, $\mathbf{M}$ is a $(\mathrm{n}\times 1)$ column vector, where each row is $\mathbf{M_i}$. Further, $\mathbf{M_i}$ is the moment about the wire tensions at the i^{th} rolling contact point and is expressed as the product of the distance from the rolling contact point to the wire ($\mathbf{d_i}$) and tension ($\mathbf{T}$). The tension $\mathbf{T}$ is a (2×1) column vector, where each row is $\mathrm{T_a}$ and $\mathrm{T_b}$. These are expressed as

$$\begin{aligned}h_\mathrm{i} = Rcos\left(\textstyle\sum_{\mathrm{j=i+1}}^{\mathrm{n}}\theta_\mathrm{j} - \frac{\theta_{\mathrm{i+1}}}{2}\right) + (H_i - 2R)\cos\left(\textstyle\sum_{\mathrm{j=i+1}}^{\mathrm{n}}\theta_\mathrm{j}\right) \\ + Rcos\left(\textstyle\sum_{\mathrm{j=i+1}}^{\mathrm{n}}\theta_\mathrm{j} + \frac{\theta_\mathrm{i}}{2}\right)\end{aligned} \quad (5)$$

$$\mathbf{M_i} = \mathbf{d_i}\mathbf{T} \quad (6)$$

$$\mathbf{d_i} = \begin{bmatrix} D_{ia} & D_{ib} \end{bmatrix} = \begin{bmatrix} D(\theta_i) & D(-\theta_i) \end{bmatrix} \quad (7)$$

$$\mathbf{T_i} = \begin{bmatrix} T_a & T_b \end{bmatrix}^T \quad (8)$$

B. Payload Analysis

To analyze the payload, we assume that we have a simple surgical instrument, n = 2. Then, the moment equilibrium equation (4) is developed as follows.

$$\begin{cases} (h_1 + h_2)\mathrm{F} = -T_a D_{1a} + T_b D_{1b} \\ h_2 \mathrm{F} = -T_a D_{2a} + T_b D_{2b} \end{cases} \quad (9)$$

To summarize this for F,

$$\begin{cases} \mathrm{F} = \frac{-T_a D_{1a} + T_b D_{1b}}{h_1 + h_2} \\ \mathrm{F} = \frac{-T_a D_{2a} + T_b D_{2b}}{h_2} \end{cases} \quad (10)$$

If no payload (F = 0) is required, d_1 must be equal to d_2. This implies that each joint always moves at the same angle. However, when the payload is required, the joints have different angles depending on the magnitude of the payload and tensions. To confirm this, the payload that satisfies equation (10) is plotted against θ_1 and θ_2 with randomly assigned variables (Fig. 3). When the base tensions are kept constant, the angles of the joints are determined according to the payload. Given this behavior, we considered a method to raise the payload curve with respect to the payload axis. This implies that we need to maximize the payload by optimizing the design variables of the rolling joint.

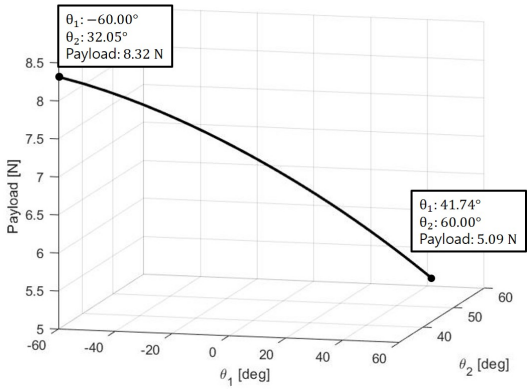

Fig. 3. Payload distributions with randomly assigned variables, when n = 2 and ($H_1 = 30$ mm, $H_2 = 35$ mm, R = 10 mm, B = 3 mm, d = 8 mm, $T_a =$ 50 N, and $T_b = 0$ N,). It is assumed that T_b is zero because the bending direction dominates the stretching direction in the bending.

C. Objective Function

The goal of optimization is to minimize the objective function with the 2-norm of the inverse of the payload. The payload function is composed of design variables, and therefore, the variables to be determined through optimization are R, B, and H. When $n = 2$, the payload is represented by two equations through (4), and when $n = x$, the payload is represented by x equations. It does not matter which of the payloads is used as the objective function.

$$min \left\| \frac{1}{F} \right\|^2 = \left\| \frac{\mathrm{h_1 + h_2}}{-\mathrm{T_{1a}D_{1a} + T_{1b}D_{1b}}} \right\|^2$$
$$(or) = \left\| \frac{\mathrm{h_2}}{-\mathrm{T_{2a}D_{2a} + T_{2b}D_{2b}}} \right\|^2, \ (n = 2) \quad (11)$$

D. Constraints for the Optimization

When optimizing the payload, there are four major constraints that arise from the geometrical structure of the instrument.

(1) Maximum range of the joint angle

The range of one joint should be the total required angle (θ_{req}) divided by n. In this study, θ_{req} is 120 degrees.

$$-\frac{\theta_{req}}{n} \le \theta_i \le \frac{\theta_{req}}{n} \quad (12)$$

(2) Working range of the rolling surface

The joint must have sufficient rolling surface to rotate to the maximum angle. In other words, the distance from the center of the joint to the rolling contact point at the maximum rotation must be smaller than the distance from the center of the joint to the wire (Fig. 4).

$$R \sin\left(\frac{\theta_{req}}{2n}\right) \le d \quad (13)$$

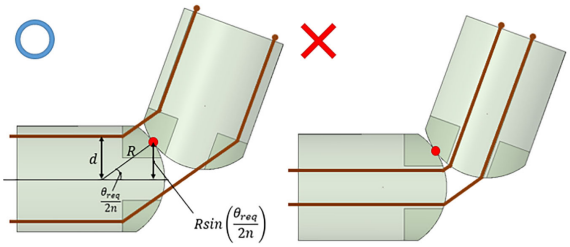

Fig. 4. Constraint of working range of the rolling surface

(3) Minimum step depth of wire

The distance of the wire hole from the top of the rolling surface (B) must be greater than the distance from the rolling contact point at maximum rolling to the top of the rolling surface (Fig. 5).

$$R\left[1 - cos\left(\frac{\theta_{req}}{2n}\right)\right] \le B \quad (14)$$

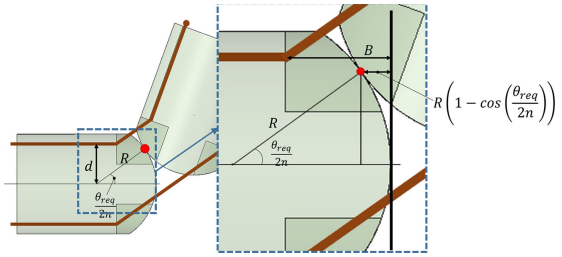

Fig. 5. Constraint of the minimum step depth of the wire

(4) Radius of curvature

To use a surgical instrument with an existing endoscope or a new endoscopic system, the radius of curvature at its maximum bending should be less than or equal to the minimum radius of a conventional endoscope. In contrast, to access the area under an endoscope or in a new endoscopic system, the minimum radius of curvature of the instrument should be larger than the sum of the diameter of the endoscope and the instrument radius. The radius of curvature was obtained using the similarity of the blue and yellow triangles shown in Fig. 6. In (15), α is the half of the sum of the diameter of the endoscope and the radius of the instrument, and β is the minimum radius of curvature of conventional endoscopes.

$$\rho = \frac{R\cos\left(\frac{\theta}{2n}\right) - \left(R - \frac{H}{2}\right) + R\sin\left(\frac{\theta_{req}}{2n}\right)\tan\left(\frac{\theta_{req}}{2n}\right)}{\tan\left(\frac{\theta_{req}}{2n}\right)}, \ \alpha \le \rho \le \beta \quad (15)$$

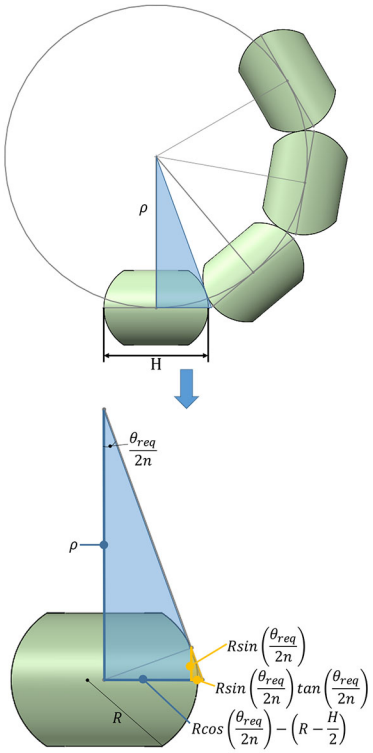

Fig. 6. Constraint of radius of curvature

(5) Wire slack protection

As mentioned in (3), the change in the total wire length differs according to the R and B. If R < B, ΔL is negative. This means that the wire will loosen and the instrument will no longer hold the current posture. As a result, it will be easily distorted by external forces. Thus, R should be larger than B.

$$R \geq B \tag{16}$$

E. Payload Optimization

Because the objective function (11) has high nonlinearity, optimization was performed using MATLAB's Global Optimization Toolbox. The 'fmincon' function was used, which is suitable for finding the minimum of a constrained nonlinear multivariable problem. As solvers, 'MultiStart' and 'GlobalSearch' was used and the results of both solvers were verified to be the same. The result of the optimization consists of the values of $R, B,$ and H that maximize the maximum payload.

The constraints mentioned in Section II-D should be modified for the inputs needed by optimization functions. The minimum step depth of the wire (14), radius of curvature (15), and wire slack protection (16) constraints were applied as nonlinear inequality conditions, and the other constraints (12, 13) were applied as lower and upper bounds. In addition, the condition that all payloads calculated by the moment equilibrium equation according to the number of joints should be equal was applied as a nonlinear equality condition.

III. Experiment and Result

A. Optimization of a Scaled-up Prototype

To validate the objective function used to calculate the payload and the optimization method, we applied the optimization method to the previously proposed concept of a surgical instrument attached to an endoscope [9]. For the convenience of calculation, it is assumed that the number of joints (n) is two, the joints only move up and down (1 DOF), and the maximum range of motion of the bending section (θ_{req}) is ± 120 degrees. The diameter of the instrument is 3.7 mm and the distance from the center of the joint to the wire (d) is 1.4 mm. The radius of curvature of the bending section should be less than 18.56 mm, which is the minimum radius of curvature of a conventional endoscope according to the specifications of commercially available endoscope parts. In addition, the radius of curvature should be greater than the half of the sum of the diameter of the endoscope and the radius of the instrument in order to enable it to reach below the endoscope. The bound of the minimum radius of curvature, including a margin, was set to 9 mm.

However, it is difficult to confirm that the optimization is properly performed under these conditions. The tension of the wires, the angle of each joint, and the payload had to be measured, but the joints were too small to be implemented in a 3.7 mm diameter instrument joint. To attach encoders on each joint to measure the actual joint angles, we scaled up all the parameters five times physically. However, the number of joints (n) and the maximum angle range of motion (θ_{req}) were not scaled up, and the diameter of the wire and wire paths were not scaled up to make the actuating environment as close to the actual one as possible.

The diameter of the prototype is 18.5 mm, and the initial values and bounds for the optimization are summarized in Table I. We used a 7×7 stranded wire cables for actuation with 0.36 mm in diameter. The tension T_a was limited by considering a safety factor of 2.0 from the maximum tensile strength of the wire cable (approximately 100 N). The optimization results of both solvers resulted in $R = 14.00$ mm, $B = 1.87$mm, and $H_1 = 47.63$ mm. When tension T_a was applied to 50.00 N, $\theta_1$was$-60.00°$, $\theta_2$was$-1.23°$, and the payload was 5.72 N (Table II).

TABLE I. Initial Conditions and Bounds for the Optimization of the Scaled-up Prototype

Initial conditions	*Bounds*
$\theta_1, \theta_2 = -60°,$ $T_a = 0\ N,$ $R = 0\ mm,$ $B = 0\ mm,$ $H_1 = 0\ mm, H_2 = 60\ mm,$ $d = 7\ mm,$ $\alpha = 45\ mm, \beta = 92.8\ mm$	$-60° \leq \theta_1, \theta_2 \leq 60°$ $0 \leq T_a \leq 50\ N$ $0 \leq R \leq \mathrm{d}/sin\left(\frac{\theta_{req}}{2n}\right)\ mm$ $0 \leq \mathrm{B} \leq \infty\ mm$ $0 \leq H_1 \leq \infty\ mm$

TABLE II. Result of the Optimization in the Proto Type

$R(mm)$	$B(mm)$	$H(mm)$	$T_a(N)$	$\theta_1(deg)$	$\theta_2(deg)$	$payload\ (N)$
14.00	1.87	47.63	50.00	-60.00	-1.23	5.72

B. Payload Verification

We set up an experimental testbed to compare the simulated optimization results with the measured using the scaled-up prototype. The prototype was built on a 3D printer and set to move horizontally (1 DOF) to eliminate the effects

of gravity. Rotary encoders (RM-08, RLS) were attached to the center of the rolling circle of each joint to obtain the angle of the joints in real-time, and load cells (333FDX, KTOYO) were applied to the driving unit to measure the tension. To apply a payload to the joint end, the wire was also used as the driving unit. In addition, the rotary encoder and the load cell were used to check whether the wire was located perpendicular to the distal joint and how much tension was applied. The testbed is shown in Fig. 7.

Considering the position and orientation of the end-effector of the joint at the joint angles obtained in Table II when a tension of 50 N was applied, the position of the driving unit for the payload was set so that the payload could act perpendicular to the wire. The experiment was started with the joints in a neutral position and the tension was applied at 5 N with pretension on both sides. The inputs were added alternately between the driving unit for the joints and the driving unit for the payload. The wire in the bending direction was then pulled and the wire in the stretching direction was partially released. When the joint was partially bent, the payload wire was pulled more so that the joints were also stretched to some extent. This was repeated until the payload reached 50N, at which time the joint angles and payload were measured.

C. *Effect of the number of joints on optimization*

In addition, we investigated the dependence of the optimization on the number of joints. Our hypothesis was that as the number of joints increase, the flexibility increases, and therefore, the stiffness and payload would decrease. To confirm this, additional optimizations were performed by increasing only the number of joints on the scaled-up prototype, and all conditions remained the same. Table IV summarizes the optimized design variables, length of the bending section, and maximum payload according to the number of joints. The length of the bending section is the distance from the center of the rolling circle of the first joint to the end tip when the joint is straightened.

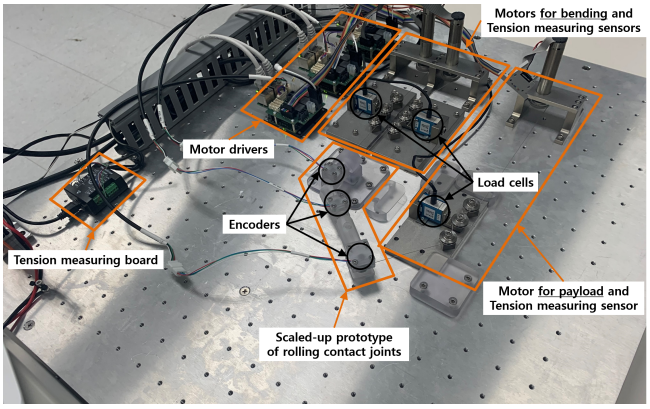

Fig. 7. Fabricated scaled-up prototype and testbed environment

TABLE III. MEASURED JOINT ANGLES AND PAYLOAD

	$T_a(N)$	$\theta_1(deg)$	$\theta_2(deg)$	$payload\ (N)$
Measured values	50.23	-59.92	1.27	5.69

TABLE IV. RESULT OF THE OPTIMIZATION ACCORTING TO THE NUMBER OF JOINTS

n	$R(mm)$	$B(mm)$	$H(mm)$	Length of bending section (mm)	$Maximum\ payload(N)$
2	14.00	1.87	47.63	121.63	5.72
3	20.47	1.23	30.13	140.73	5.68
4	27.05	0.92	22.02	153.11	5.62
5	33.67	0.74	17.63	164.19	5.57

IV. DISCUSSION

The experiment result of the payload verification shows that the measured joint angles and the payload are almost equal to the values obtained from the optimization (Table III). However, it does not guarantee that the payload obtained through optimization really the maximum payload. To confirm this, we plotted the distribution of payload with respect to θ_1 and θ_2. As can be seen in Fig. 8, the payload at the position obtained from the optimization result is identical to the payload obtained from the optimization result. Moreover, it can be visually confirmed that the position with the largest payload in the line at which the payloads intersect. Therefore, the payload obtained through optimization is the maximum payload.

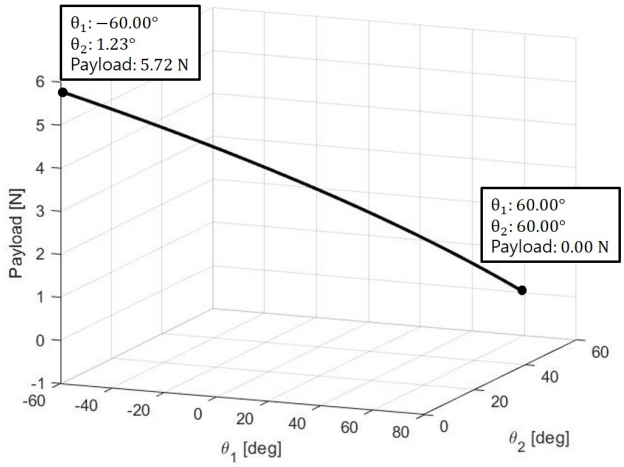

Fig. 8. Payload distributions for the optimized prototype

The optimization results according to the number of joints were as expected. As the number of joints increases, the value of R increases and that of B decreases. This is because the angle range over which one joint should rotate decreases. In addition, H gradually decreased, but the length of the entire bending section gradually increased (Table. IV). As shown in equation (9), the payload is proportional to the distance between the wire and the rolling contact point. Moreover, it is inversely proportional to the distance between the rolling contact point and the end-effector of the bending section. Thereafter, the effect of the decrease in payload due to the increase in the length of the bending section is more dominant.

V. CONCLUSION

This paper presented the optimization of the joint design variables of flexible surgical instruments to maximize payload, which was derived from the moment equilibrium equation. A scaled-up prototype was fabricated using the

design variables obtained from the optimization, and the validity of the proposed method, which calculates the payload from the moment equilibrium equations, was confirmed by showing that the payload obtained from the optimization is the same as the payload measured in the experiment. By plotting the payload distribution, it was also confirmed that the payload obtained from the optimization is the maximum. In addition, the payload tended to decrease as the number of joints increased.

This payload optimization method could also be extended to minimizing the deflection of the bending section against external forces and minimizing the diameter of the surgical instrument given the minimum required payload. To do this, the factor that is to be minimized must be represented by design variables and applied in an objective function. As further work, analysis of frictional force and other external forces will be additionally conducted and the optimization method will be extended to two DOFs.

ACKNOWLEDGMENT

This work was supported by the National Research Foundation (NRF) of Korea (Grant No. 2017H1A2A1043 159), and this work also supported by a grant of the International Joint Technology Development Project funded by the Korean Ministry of Trade, Industry and Energy (Grant No. P0006718).

REFERENCES

[1] A. N. Kalloo, V. K. Singh, S. B. Jagannath, H. Niiyama, S. L. Hill, C. A. Vaughn, C. A. Magee, S. V. Kantsevoy, Flexible transgastric peritoneoscopy: A novel approach to diagnostic and therapeutic interventions in the peritoneal cavity, Gastrointest. Endosc., vol. 60, no. 1, pp. 114-117, Jul. 2004.

[2] D. Rattner and A. Kalloo, ASGE/SAGES Working Group on Natural Orifice Translumenal Endoscopic Surgery White Paper October 2005, Gastrointest Endosc, vol. 63, no. 2, pp. 199–203, 2006.

[3] D. W. Rattner, R. Hawes, S. Schwaitzberg, M. Kochman, and L. Swanstrom, The Second SAGES/ASGE White Paper on natural orifice transluminal endoscopic surgery: 5 years of progress, Surgicalendoscopy, vol. 25, no. 8, pp. 2441–2448, 2011.

[4] S. J. Phee, A. P. Kencana, V. A. Huynh, et al., Design of a master and slave transluminal endoscopic robot for natural orifice transluminal endoscopic surgery, Proc. Inst. Mechanical Engineers, Part C: J. Mechanical Engineering Sci., vol. 224, pp. 1495–1503, 2010.

[5] D. J. Abbott, C. Becke, R. I. Rothstein, and W. J. Peine, Design of an Endoluminal NOTES Robotic System, IEEE/RSJ Int. Conf. Intelligent Robots and Systems (IROS), pp. 410 – 416, 2007.

[6] P. Berthet-Rayne, G. Gras, K. Leibrandt, P. Wisanuvej, A. Schmitz, C. A. Seneci, and G.-Z. Yang, The i2snake robotic platform for endoscopic surgery, Annals of Biomed. Engineer. 10.1007/s10439-018-2066-y, 2018.

[7] P. Mascagni, S. G. Lim, C. Fiorillo, et al., Democratizing Endoscopic Submucosal Dissection: Single-Operator Fully Robotic Colorectal Endoscopic Submucosal Dissection in a Pig Model, Gastroenterology, vol. 156, no. 6, pp. 1569-1571, 2019.

[8] M. Hwang and D. S. Kwon, K-FLEX: A flexible robotic platform for scar-free endoscopic surgery, The International Journal of Medical Robotics and Computer Assisted Surgery, vol. 16, no. 2, 2020.

[9] D. H. Lee, M. Hwang, D. S. Kwon, Robotic endoscopy system (easyEndo) with a robotic arm mountable on a conventional endoscope, IEEE International Conference on Robotics and Automation (ICRA), Montreal, Canada, May 2019

[10] P. Berthet-Rayne, K. Leibrandt, K. Kim, et al., Rolling-joint design optimization for tendon driven snake-like surgical robots, IEEE/RSJ International Conference on Intelligent Robots and Systems, (IROS), Madrid, Spain, Sep 2018

[11] K. Oliver-Butler, J. Till, and C. Rucker, Continuum robot stiffness under external loads and prescribed tendon displacements, IEEE Trans. on Robotics, vol. 35, no. 2, pp. 403–419, 2019.

[12] J. Suh, K. Kim, J. Jeong, and J. Lee, Design Considerations for a Hyper-Redundant Pulleyless Rolling Joint With Elastic Fixtures, IEEE/ASME Trans. Mechatronics, vol. 20, no. 6, pp. 2841-2852, 2015.

[13] J. W. Suh J. J. Lee D. S. Kwon, Underactuated miniature bending joint composed of serial pulleyless rolling joints, Adv. Robot., vol. 28, no. 1, pp. 1-14, 2014.

[14] M. Hwang, D. S. Kwon, Strong continuum manipulator for flexible endoscopic surgery, IEEE/ASME Trans. Mech., vol. 24, no. 5, pp. 2193–2203, 2019.

[15] S. M. Segreti, M. D. M. Kutzer, R. J. Murphy, and M. Armand, Cable Length Estimation for a Compliant Surgical Manipulator, IEEE International Conference on Robotics and Automation (ICRA), Minnesota, USA, May 2012.

[16] D. Haraguchi, T. Kanno, K. Tadano, and K. Kawashima, A Pneumatically Driven Surgical Manipulator With a Flexible Distal Joint Capable of Force Sensing, IEEE/ASME Transactions on Mechatronics, Vol. 20, No. 6, pp. 2950-2961, Dec. 2015.

[17] J. Ding, R. E. Goldman, K. Xu, P. K. Allen, D. L. Fowler, and N. Simaan, Design and Coordination Kinematics of an Insertable Robotic Effectors Platform for Singe-Port Access Surgery, IEEE/ASME Trans. Mechatronics, vol. 18, no. 5, pp. 1612-1624, Oct. 2013.

[18] T. Kanno, D. Haraguchi, M. Yamamoto, K. Tadano, and K. Kawashima, A Forceps Manipulator With Flexible 4-DOF Mechanism for Laparoscopic Surgery, IEEE/ASME Trans. Mechatronics, vol. 20, no. 3, pp. 1170-1178, June 2015.

[19] A. Gao, R. J. Murphy, H. Liu, I. I. Iordachita, and M. Armand, Mechanical Model of Dexterous Continuum Manipulators With Compliant Joints and Tendon/External Force Interactions, IEEE Trans. Robot., vol. 22, no. 1, pp. 465-475, Feb. 2017.

[20] D.B.Camarillo,C. F.Milne, C. R. Carlson, M. R. Zinn, and J.K. Salisbury, Mechanics modeling of tendon-driven continuum manipulators, IEEE Trans. Robot., vol. 24, no. 6, pp. 1262–1273, Oct. 2008.

[21] K. Harada, K. Tsubouchi, M. G. Fujie, and T. Chiba, Micro Manipulators for Intrauterine Fetal Surgery in an Open MRI, IEEE International Conference on Robotics and Automation (ICRA), Barcelona, Spain, April 2005

[22] F. V. Meer, A. Giraud, D. Esteve, X. Dolla, A disposable plastic compact wrist for smart minimally invasive surgical tools, IEEE/RSJ International Conference Intelligent Robot and Systems (IROS), pp. 919–924, Alberta, 2005

[23] C. Martin, F. Chapelle, J. J. Lemaire, G. Gogu, Neurosurgical robot design and interactive motion planning for resection task, IEEE/RSJ International Conference Intelligent Robot Systems (IROS), pp. 4505–4510, St. Louis, 2009.

[24] G. Cooper, D. T. Wallace, S. Chang, S. C. Anderson, D. Williams, and S. Manzo, Surgical tool having positively positionable tendon-actuated multi-disk wrist joint, U.S. Patent, 6817974 B2, Nov. 16, 2004.

[25] M. R. Williams, Instrument wrist with cycloidal surfaces, U.S. Patent 20110152879 A1, Dec. 22, 2011.